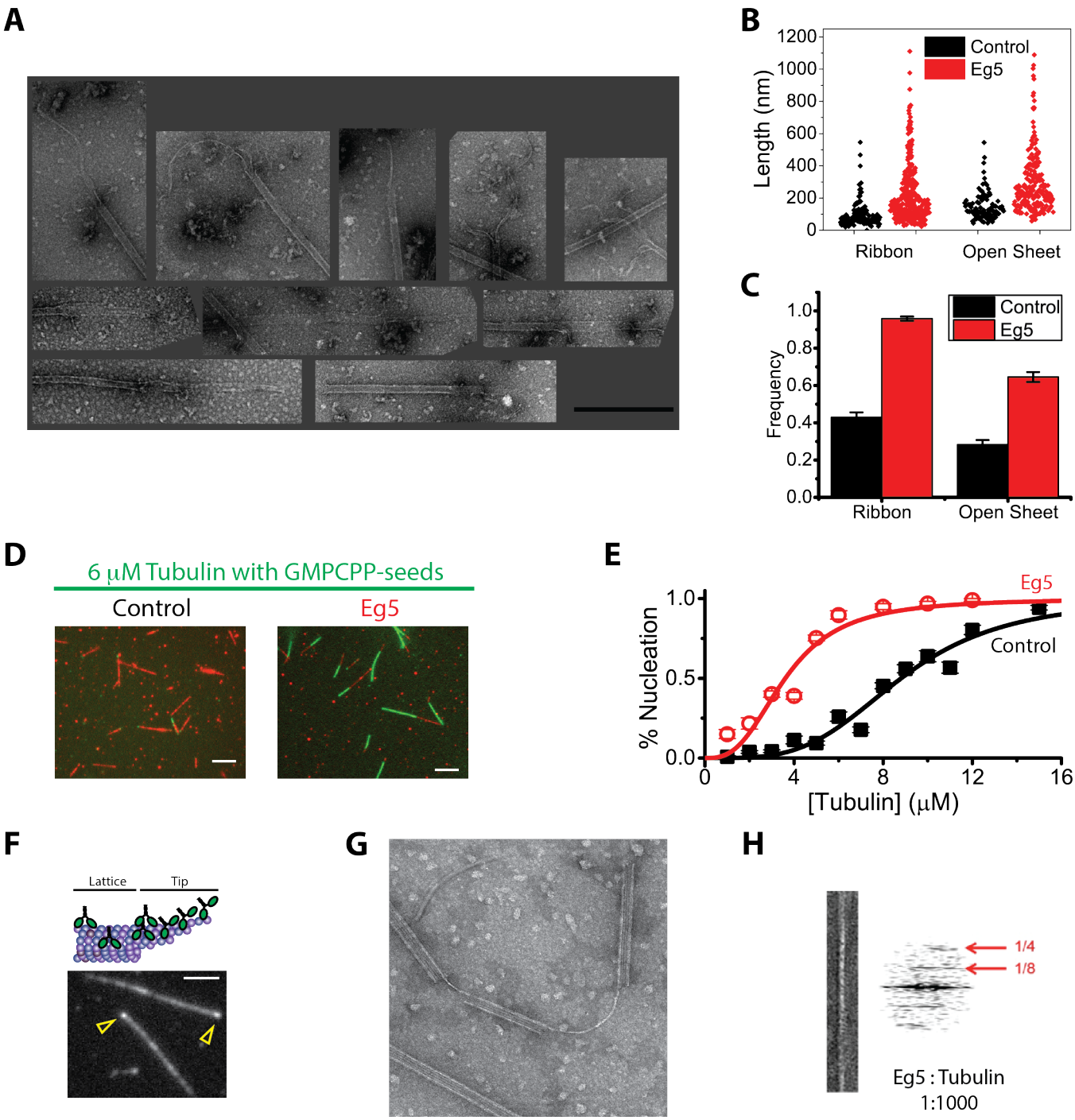

Figure S1. Eg5 motors induce template-based nucleation. Related to Figure 1. (A) Gallery of negative-stain EM images of ribbons and sheets at ends of microtubules polymerized in the presence of Eg5 motors. Scale bar is 400 nm. (B) Distribution of ribbon and sheet lengths (plotted as mean and SEM in **Figure 1D**). (C) Frequency of ribbons and sheets counted on microtubule ends in the presence and absence of Eg5 motors (error from counting statistics is sqrt(f*(1-f)/n), where n = 46-303 and f is the fraction of events). (D) Epi-fluorescence images of TMR-labeled microtubules elongation on Cy5-labeled GMPPCP-seeds in the presence or absence of 130 nM unlabeled Eg5 dimers (mean ± SEM; n = 109-713). Scale bar: 5 μm. (E) Fraction of tip-nucleated microtubules as a function of initial free tubulin concentration. (F-H) Eg5 motors accumulate at the microtubule plus-ends. (F) Schematic and TIRF image of GFP-labeled Eg5 motors accumulating at the plus-end of a GMPCPP-stabilized microtubule. Open arrows indicate Eg5 end-bulbs. Scale bar: 2 μm. (G) Negative-stain EM image of microtubules grown at 1:1000 Eg5:tubulin stoichiometry showing lattice and isolated protofilament ribbons. (H) Diffraction pattern of a straightened protofilament ribbon from (G). The strong 8 nm layer line observed is indicative of the motor decorating the protofilaments following the tubulin axial periodicity.

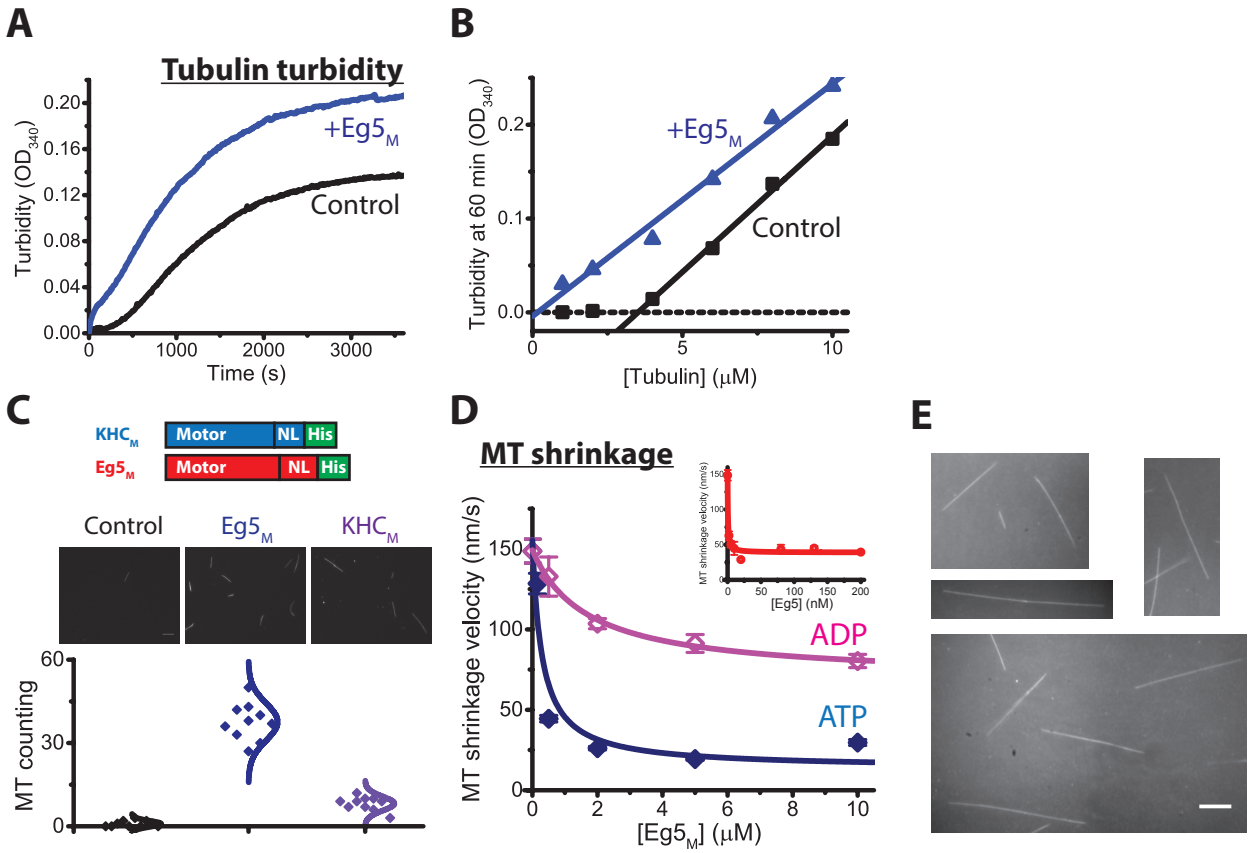

Figure S2. Eg5 monomers promote microtubule nucleation and stability. Related to Figure 2. (A) Averaged turbidity traces of 8 μM free tubulin polymerizing in the presence and absence of 2 μM Eg5 monomers, revealing that Eg5 promotes nucleation rate with a higher turbidity plateau (n = 3-5 traces). Turbidity carried out at 37 °C with 10% added DMSO. (B) Turbidity signal at 1 hour across tubulin concentrations demonstrating that monomeric Eg5 motors reduces critical concentration of tubulin polymerization. (C) Effect of $Eg5_M$ and KHC_M on microtubule nucleation. (Top) Diagrams monomeric motors, generated by truncating the respective coiled-coil domains and fusing to a C-terminal His-tag [S1]. (Middle) Images of microtubules nucleated in the absence or presence 2 μM monomeric motors plus 5 μM tubulin in the BRB80 solution containing 2.5 mM Mg-GTP, 5 mM Mg-ATP, 5 mM additional $MgCl_2$, and 10% DMSO. (Bottom) Numbers of microtubules counted per screen for the three conditions (see Methods for details of microtubule counting assay). (D) Effect of $Eg5_M$ on microtubule shrinkage rates; catastrophes were induced by washing out free tubulin. The motor concentrations at half-max stabilization gave $K_{0.5}$ of 1.7 ± 0.3 nM $Eg5_M$ in 5 mM ADP and $K_{0.5}$ = 0.3 ± 0.18 nM $Eg5_M$ in 5 mM ATP. Inset: similar curve for effect of dimeric Eg5 on the dilution-induced microtubule shrinkage rate in 5 mM ATP. (E) Representative images of unlabeled taxol-stabilized microtubules in 500 nM $Eg5_M$-GFP and 1 mM ATP, showing there is no preferential binding or accumulation of the monomer at microtubule ends (contrast with plus-end accumulation of dimer in **Figure S1F** and **G**). Scale bar is 5 μm.

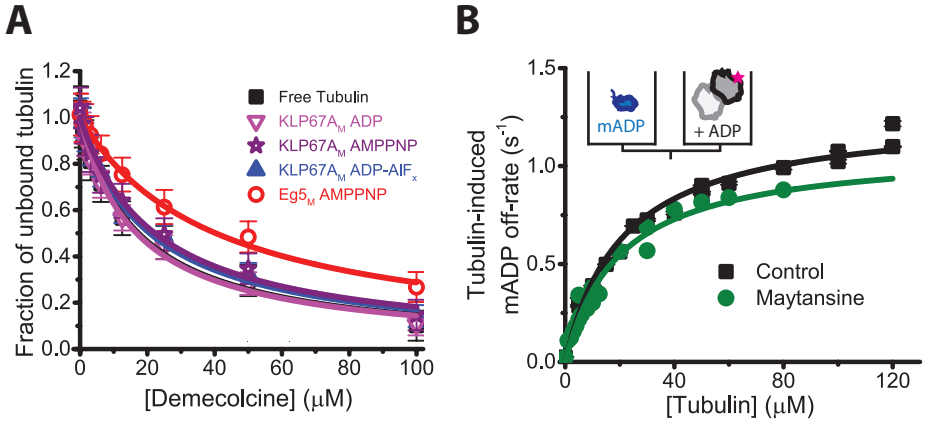

Figure S3. Eg5-modulated tubulin straightening perturbs colchicine-tubulin binding strength. Related to Figure 3. (A) Entire demecolcine binding isotherms shown in **Figure 3D**. (B) Tubulin-induced mantADP release in the presence and absence of Maytansine. $K_{0.5}$. Control: $K_{0.5}$ = 21 ± 8 μM, k_{max} = 1.3 ± 0.2 s^{-1}; Maytansine: $K_{0.5}$ = 20 ± 3 μM, k_{max} = 1.1 ± 0.07 s^{-1}.

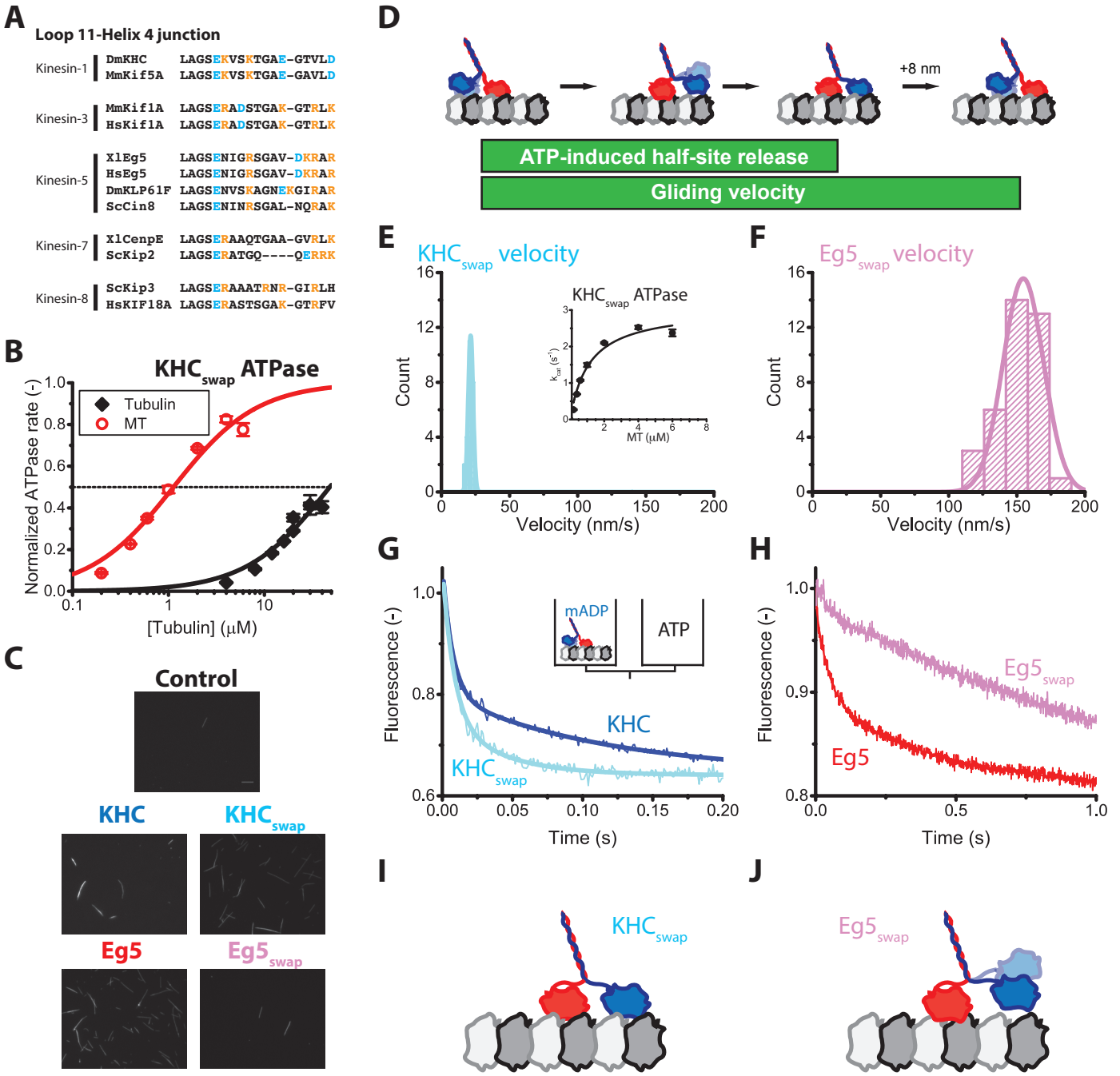

Figure S4. L11α4 -mediated motor activity and microtubule stability. Related to Figure 4. (A) Sequence alignment of kinesin-1, -3, -5, -7, and -8 motors. (B) Tubulin- and microtubule-stimulated ATPase of monomeric KHC_{swap}, normalized to their maximal values. The K_M were 48 ± 24 μM and 1.1 ± 0.2 μ M for tubulin and microtubules, respectively, suggesting that Eg5 motors favor straight microtubule lattices 40-fold over curved, soluble tubulin (mean ± SEM; n_{MT} = 5; n_{Tub} = 3). (C) Representative images of number of microtubules formed under varying motor species (raw data for **Figure 4E**). (D-J) Loop11 regulates kinetic transitions in the kinesin mechanochemical cycle. (D) Three-state model includes motor one-head-bound and two-heads-bound transitions [S2]. ATP-induced half-site release assays, in which mantADP-incubated one-head-bound motors are flushed against 2 mM ATP to release the tethered-head fluorescence signal, contain the transition time from the one-head-bound state to the two-heads-bound state [S3, S4]. The gliding velocity divided by its 8-nm step-size gives the motor stepping rate, and its reciprocal gives the stepping cycle time. The duration between the transient kinetics and the steady-state reaction time confers the reaction time of rear-head detachment. (E and F) Microtubule gliding assays of Loop11-swapped mutants (21 ± 2 nm/s for KHC_{swap} and 155 ± 15 nm/s for $Eg5_{swap}$; n= 26-37, mean ± SD). The stepping times of KHC_{swap} and $Eg5_{swap}$ were thus 381 ± 36 msec and 52 ± 5 msec, respectively. Inset: Microtubule-stimulated ATPase of KHC_{swap} with Michaelis-Menten fit gives k_{cat} of 3.1 ± 0.2 s^{-1} (or a 323 msec cycle time) and K_M of 1.1 ± 0.2 μM. The similarity of the 381 msec step time and 323 msec ATPase cycle time demonstrates ATP hydrolysis remains tightly coupled to stepping in the KHC_{swap} mutant. (G and H) ATP-induced half-site release assays of dimeric KHC and Eg5 motors. The averaged traces were fit to a biexponential, where the rate of the fast phase corresponds to the first-passage time of the tethered-head touchdown (which triggers mantADP release and fall in fluorescence) [S4]. N = 5-7 experiments for each determination. For KHC in panel (G), inverting the fitted half-site release rates of 140 ± 6 s^{-1} and 123 ± 11 s^{-1}, gives tethered-head binding times of 7 ± 0.3 msec and 8 ± 0.7 msec for KHC and KHC_{swap}, respectively. For Eg5 in panel (H), inverting the fitted half-site rates of 24 ± 1 s^{-1} and 26 ± 3 s^{-1} gives tethered-head binding times of 42 ± 2 msec and 38 ± 4 msec for Eg5 and $Eg5_{swap}$, respectively. Thus, for both KHC and Eg5, swapping L11α4 does not alter

the transition time from the one-head-bound state to the two-heads-bound state, despite changes in the motor stepping rate. (I and J) Diagram of the dominant state of the two L11-α4 mutants. From comparison of tethered head binding rates and motor stepping rates, KHC_{swap} motors spend ~98% of their cycle in the two-heads-bound state, whereas $Eg5_{swap}$ motors spend 73% of their cycle in the one-head-bound state.

Rate constants	Description	Source	Value	Unit
Parameters for microtubule dynamics				
k_{on}	Longitudinal tubulin-tubulin on-rate	Constrained¶	8.45	$\mu M^{-1}s^{-1}$ per MT
k_{off}^{GTP}	Longitudinal tubulin off-rate in GTP	Constrained¶	5	s^{-1}
k_{off}^{GDP}	Longitudinal tubulin off-rate in GDP	Constrained¶	5	s^{-1}
k_{zip}	Lateral bond annealing rate§	Constrained¶	10	s^{-1}
k_{unzip}	Lateral bond breaking rate§	Constrained¶	30	s^{-1}
k_{hyd}	Tubulin GTP hydrolysis rate	Adapted from [S5]	0.05	s^{-1}
F_{GTP}	GTP-induced lateral bond stabilization factor	Constrained¶	2.5	fold
F_{wall}	Mechanical stabilization by Mt lattice	Adapted from [S6]	9	fold
Parameters for dimeric Eg5-microtubule interaction				
k_{on}^{Motor}	Eg5-microtubule binding rate	Adapted from [S7]	20	$\mu M\ MT^{-1}s^{-1}$
k_{step}	Eg5 stepping rate	Adapted from [S7]	10	s^{-1}
k_{unbind}	Eg5-microtubule unbinding rate	Adapted from [S1]	0.25	s^{-1}
k_{slow}	Eg5 stepping rate on curved protofilaments	Constrained by **Figure 3G**	1	s^{-1}
k_{pause}	Eg5 unbinding rate on curved protofilaments	Adapted from [S1]	0.1	s^{-1}
Parameters for monomeric Eg5-microtubule interaction				
k_{on}^{Motor}	$Eg5_M$-microtubule binding rate	Adapted from [S7]	10	$\mu M\ MT^{-1}s^{-1}$
k_{unbind}	$Eg5_M$-microtubule unbinding rate	Adapted from [S7]	10	s^{-1}
k_{pause}	$Eg5_M$ unbinding rate on curved protofilaments	Adapted from [S1]	0.1	s^{-1}
Parameters for Eg5-induced microtubule polymerization				
F_{unzip}^{Eg5}	Eg5 slowing of tubulin straight-to-curved transition rate§	Constrained by **Figure 2F**	2.2	fold

Table S1. Parameters for Eg5-stimulated microtubule polymerization model. Related to Figure 5.

¶: Parameters for simulating microtubule dynamics were trained by MT growth assays (**Figure 2E**), GDP-MT shrinkage assays (**Figure 2F**), GMPCPP-MT shrinkage rate [S1], and fray size in both growing and shrinking microtubules [S8]. Beyond setting the lateral bond zipping rate for GDP-tubulin into a GDP-lattice to zero, no additional degrees of freedom were required. §: Lateral bond formation occurs immediately upon straightening, and tubulin straight-to-curved transition occurs immediately once both lateral bonds dissociate.

Description		Association rate (k_{on})	Dissociation rate (k_{off})	Dissociation constant (K_D)	Free energy (ΔG^*)
Thermodynamics of microtubule dynamics					
Longitudinal	GTP	0.15 ($\mu M^{-1}s^{-1}$)	5 (s^{-1})	3.3×10^{-6} M	-12.6 k_BT
	GDP	0.15 ($\mu M^{-1}s^{-1}$)	5 (s^{-1})	3.3×10^{-6} M	-12.6 k_BT
Lateral	GDP|GDP	0	30 (s^{-1})	NA	NA
	GDP|GTP¶	10 (s^{-1})	12 (s^{-1})	1.2	0.2 k_BT
	GTP|GTP	10 (s^{-1})	4.8 (s^{-1})	0.48	-0.7 k_BT
Lateral, wall§	GDP|GDP	0	3.3 (s^{-1})	NA	NA
	GDP|GTP¶	10 (s^{-1})	1.3 (s^{-1})	0.13	-2.0 k_BT
	GTP|GTP	10 (s^{-1})	0.5 (s^{-1})	0.05	-3.0 k_BT
Contribution of each Eg5 motor domain adjacent to the affected lateral bond					-0.8 k_BT

Table S2. Kinetics and free energy of tubulin lattice. Related to Figure 5.

¶: Ignores any effects of the microtubule seam.
§: Wall denotes the lateral zipping process between the two sheets or bundles.

Supplemental References:

S1. Chen, Y., and Hancock, W. O. (2015). Kinesin-5 is a microtubule polymerase. Nat. Commun. *6*, 8160.

S2. Andreasson, J. O. L., Milic, B., Chen, G.-Y., Guydosh, N. R., Hancock, W. O., and Block, S. M. (2015). Examining kinesin processivity within a general gating framework. Elife *4*, e07403.

S3. Hackney, D. D. (1994). Evidence for alternating head catalysis by kinesin during microtubule-stimulated ATP hydrolysis. Proc. Natl. Acad. Sci. *91*, 6865–6869.

S4. Chen, G.-Y., Arginteanu, D. F. J., and Hancock, W. O. (2015). Processivity of the Kinesin-2 KIF3A Results From Rear-Head Gating and Not Front-Head Gating. J. Biol. Chem. *290*, 10274–10294.

S5. Melki, R., Stéphane, F., and Carlier, M.-F. (1996). Continuous Monitoring of P i Release Following Nucleotide Hydrolysis in Actin or Tubulin Assembly Using 2-Amino-6-mercapto-7-methylpurine Ribonucleoside and Purine-Nucleoside Phosphorylase as an Enzyme-Linked Assay. Biochemistry *35*, 12038–12045.

S6. Margolin, G., Gregoretti, I. V., Cickovski, T. M., Li, C., Shi, W., Alber, M. S., and Goodson, H. V. (2012). The mechanisms of microtubule catastrophe and rescue: implications from analysis of a dimer-scale computational model. Mol. Biol. Cell *23*, 642–656.

S7. Chen, G.-Y., Mickolajczyk, K. J., and Hancock, W. O. (2016). The Kinesin-5 Chemomechanical Cycle is Dominated by a Two-heads-bound State. J. Biol. Chem. *291*, 20283–20294.

S8. McIntosh, J. R., Toole, E. O., Morgan, G., Austin, J., Ulyanov, E., Ataullakhanov, F., and Gudimchuk, N. (2018). Microtubules grow by the addition of bent guanosine triphosphate tubulin to the tips of curved protofilaments. J. Cell Biol. *217*, 2691–2708.